scientific reports

Check for updates

OPEN

Rapid, high-sensitivity detection of biomolecules using dual-comb biosensing

Shogo Miyamura[1,9], Ryo Oe[1,9], Takuya Nakahara[1], Hidenori Koresawa[1], Shota Okada[2], Shuji Taue[3], Yu Tokizane[4], Takeo Minamikawa[5], Taka-Aki Yano[4], Kunihiro Otsuka[5,6], Ayuko Sakane[5,7], Takuya Sasaki[5,7], Koji Yasutomo[5,6], Taira Kajisa[5,8]✉ & Takeshi Yasui[4]✉

Rapid, sensitive detection of biomolecules is important for biosensing of infectious pathogens as well as biomarkers and pollutants. For example, biosensing of severe acute respiratory syndrome coronavirus 2 (SARS-CoV-2) is still strongly required for the fight against coronavirus disease 2019 (COVID-19) pandemic. Here, we aim to achieve the rapid and sensitive detection of SARS-CoV-2 nucleocapsid protein antigen by enhancing the performance of optical biosensing based on optical frequency combs (OFC). The virus-concentration-dependent optical spectrum shift produced by antigen–antibody interactions is transformed into a photonic radio-frequency (RF) shift by a frequency conversion between the optical and RF regions in the OFC, facilitating rapid and sensitive detection with well-established electrical frequency measurements. Furthermore, active-dummy temperature-drift compensation with a dual-comb configuration enables the very small change in the virus-concentration-dependent signal to be extracted from the large, variable background signal caused by temperature disturbance. The achieved performance of dual-comb biosensing will greatly enhance the applicability of biosensors to viruses, biomarkers, environmental hormones, and so on.

Biosensors are biomolecular sensors that utilize or imitate the skillful molecular identification function of living organisms; they are applied to a wide range of fields such as medical care, food industry, and environmental monitoring. Yet, further enhancement of biosensing performance is still required in the field of infectious pathogens as well as biomarkers, pollutant, bacteria, and environmental hormones. For example, one timely and urgent application that benefits from improved performance is still testing of coronavirus disease 2019 (COVID-19) because COVID-19, caused by severe acute respiratory syndrome coronavirus 2 (SARS-CoV-2), has rapidly spread and is still occurring all over the world. While reverse-transcription polymerase chain reaction (RT-PCR)[1–3] has been widely used as a current standard for COVID-19 testing in clinical practice, research has also been conducted on biosensors of SARS-CoV-2, vigorously. The potential methods that may improve the biosensing performance is the use of optical biosensors[4,5] due to both rapidity and high sensitivity. For example, optical biosensors based on surface plasmon resonance (SPR)[6,7] have been widely used for analyzing biomolecules and viruses; in this technique, the spectral shift of the SPR trough in the wavelength or angular spectrum is measured because the spectral shift depends on a sample concentration due to a combined effect of SPR and molecular identification function on the sensor surface. SPR analysis enables the real-time, label-free analysis of intermolecular interaction or combination by measuring a sample-concentration-dependent optical spectral shift; thus, this technique has been widely applied for the detection of various infectious pathogens such as human immunodeficiency virus [8], Ebola virus[9], norovirus[10], influenza virus[11], and even SARS-CoV-2[12–14] as

[1]Graduate School of Advanced Technology and Science, Tokushima University, 2-1 Minami-Josanjima, Tokushima, Tokushima 770-8506, Japan. [2]Graduate School of Sciences and Technology for Innovation, Tokushima University, 2-1 Minami-Josanjima, Tokushima, Tokushima 770-8506, Japan. [3]School of System Engineering, Kochi University of Technology, 185 Miyanokuchi, Tosayamada, Kami, Kochi 782-8502, Japan. [4]Division of Next-Generation Photonics, Institute of Post-LED Photonics (pLED), Tokushima University, 2-1 Minami-Josanjima, Tokushima, Tokushima 770-8506, Japan. [5]Division of Interdisciplinary Researches for Medicine and Photonics, Institute of Post-LED Photonics (pLED), Tokushima University, 2-1 Minami-Josanjima, Tokushima, Tokushima 770-8506, Japan. [6]Department of Immunology and Parasitology, Graduate School of Medicine, Tokushima University, 3-18-15 Kuramoto, Tokushima, Tokushima 770-8503, Japan. [7]Department of Biochemistry, Graduate School of Medicine, Tokushima University, 3-18-15 Kuramoto, Tokushima, Tokushima 770-8503, Japan. [8]Graduate School of Interdisciplinary New Science, Toyo University, 2100 Kujirai, Kawagoe, Saitama 350-8585, Japan. [9]These authors contributed equally: Shogo Miyamura and Ryo Oe. ✉email: kajisa@toyo.jp; yasui.takeshi@tokushima-u.ac.jp

well as various biomarkers such as proteins[15,16], DNA[17,18], and whole cells[19,20]. The limit of detection (LOD) for SARS-CoV-2 nucleocapsid protein (N protein) antigen has reached 85 fM or 4 pg/ml[14]; however, in order to measure clinical samples (for example, human nasopharyngeal aspirates), further improvement in LOD (to the fM level or sub-fM level) is necessary[21]. A reason for the limited sensitivity in SPR is an optical instrumentation resolution as well as a relatively broad spectrum of SPR trough compared to its slight spectrum shift. Optical biosensing techniques, such as fluorescence[22,23] and surface-enhanced Raman scattering (SERS)[24,25], could be another potential candidate for the biosensing of SARS-CoV-2. For instance, a combination of SERS with antibody pair, SERS-active hollow Au nanoparticles, and magnetic beads achieved LOD of 2.56 fg/mL for the SARS-CoV-2 antigen, facilitating the identification of SARS-CoV-2 in human nasopharyngeal aspirates within 30 min[21]. While the discrimination of infection has been achieved, the Raman signals of samples diagnosed as negative still show variations among samples, which may lead to potential misdiagnosis between false positive and true negative during the early stages of infection.

Regarding the limitation of optical instrumentation resolution in SPR, if this sample-concentration-dependent optical spectral shift is transformed into a photonic radio-frequency (RF) signal, then such photonic RF biosensing would benefit from the high precision and real-time nature provided by well-established electric frequency measurements with RF frequency standards and measurement apparatuses. Recently, optical frequency combs (OFCs)[26–29] have attracted attention for use as photonic RF sensors based on a frequency conversion function between the optical and RF regions[30,31]. OFC is composed of a series of optical frequency modes (freq. = ν_m) with a constant mode spacing of f_{rep} in the RF band. A relation between ν_m and f_{rep} is given by

$$\nu_m = f_{ceo} + mf_{rep}, \tag{1}$$

where f_{ceo} is a carrier-envelope-offset frequency and m is mode number. Since f_{rep} is a RF signal, OFC acts as an accurate frequency converter between optical and electrical regions. For example, a refractive-index-dependent (RI-dependent) optical spectrum shift was converted into a change in f_{rep} of around several tens of MHz by placing a multimode-interference (MMI) fiber sensor[32,33] inside a fiber OFC cavity[34–36]. Then, the f_{rep} signal with the spectral linewidth below 1 Hz was rapidly and precisely measured by a RF frequency counter. Furthermore, the intracavity fiber sensor enables multiple interactions between the sample and the light, enhancing the sensitivity. Due to the precise electric-measurement of the narrow-linewidth, sensitivity-enhanced f_{rep} signal, this RI-sensing OFC enables precise measurement of the sample RI with a resolution of 4.88×10^{-6} refractive index units (RIU)[34], which is two orders of magnitude better than that of the previous study of RI sensing with MMI fiber sensor[32]. Such high-sensitivity RI-sensing OFCs would have the potential to be further extended to optical biosensing, namely, to biosensing OFCs, through surface modification of the MMI fiber sensor with the molecular identification layer in terms of biomolecule interactions, similar to the surface modification employed in SPR. However, there are no attempts to apply this RI-sensing OFC for optical biosensing because the residual temperature drift of the f_{rep} signal (typically, a few hundreds Hz/hour) is still larger than the sample-concentration-dependent f_{rep} shift in biosensing (typically, a few to a few tens Hz), reducing the precision and hindering its extension to the biosensing OFC. It is essential to largely reduce the temperature drift of f_{rep} in order to open the door for the biosensing OFC.

Thus, in this article, we first developed a dual-comb configuration with an active sensing OFC and a dummy sensing OFC to suppress the temperature drift of the f_{rep} signal, namely, dual-comb biosensing; this function is similar to the active-dummy temperature compensation of strain sensors. Then, for preliminarily test of dual-comb biosensing, we applied the active-dummy dual sensing OFCs to RI sensing of a glycerol solution, which is a stable standard substance without volatilization. Finally, for proof of concept using biomolecules, we demonstrate rapid detection of the SARS-CoV-2 N protein antigen by combining the active-dummy dual sensing OFCs and surface modification of a SARS-CoV-2 N protein antibody. Prior to using real samples of SARS-CoV-2, to assess the net performance of dual-comb biosensing alone without the help of specific enhancing techniques regarding antigen–antibody interactions and/or surface modifications, commercially available, purified SARS-CoV-2 N protein antigen diluted in phosphate-buffered saline (PBS) was detected by a help of a commercially available SARS-CoV-2 N protein antibody. Since the dual-comb biosensing can be implemented with a wide variety of surface modifications for other viruses/pathogens and biological molecules, it greatly enhances the applicability of optical biosensors for virus, bacteria, protein, biomarker, environmental hormone, and so on.

Results

General principle of operation. In this study, we sought to design a biosensor that combines photonic-to-RF conversion and antigen–antibody interaction in an OFC. The biosensing OFC operates through three steps: Step (1) antigen–antibody interactions on the antibody-modified sensor surface, Step (2) RI-dependent optical spectrum shift of OFC provided by the intracavity MMI fiber sensor, and Step (3) photonic-to-RF conversion by the wavelength dispersion of the fiber cavity, as depicted in Fig. 1a. In Step (1), the selective combination of a target antigen with the corresponding antibody changes the effective RI near the sensor surface depending on the antigen concentration. In Step (2), since the intracavity MMI fiber sensor transmits only certain wavelength (λ_{MMI}) light based on its RI due to MMI and the Goos-Hänchen shift, the OFC shows an RI-dependent and hence an antigen-concentration-dependent shift in the optical spectrum. Simultaneously, the intracavity MMI fiber sensor enhances the sensing sensitivity by multiple interactions between light and sample inside the OFC cavity. The functions of Steps (1) and (2) are implemented by an intracavity MMI fiber sensor with antibody surface modification, as shown in Fig. 1b. In Step (3), the antigen-concentration-dependent shift in the optical spectrum is converted to a shift in the optical cavity length nL, where n and L are the RI and the physical length of the OFC cavity fiber, via the wavelength dispersion of RI in the cavity fiber. Finally, the change in the antigen concentration can be read out as the f_{rep} shift via $f_{rep} = c/nL$, where c is the velocity of light in a vacuum.

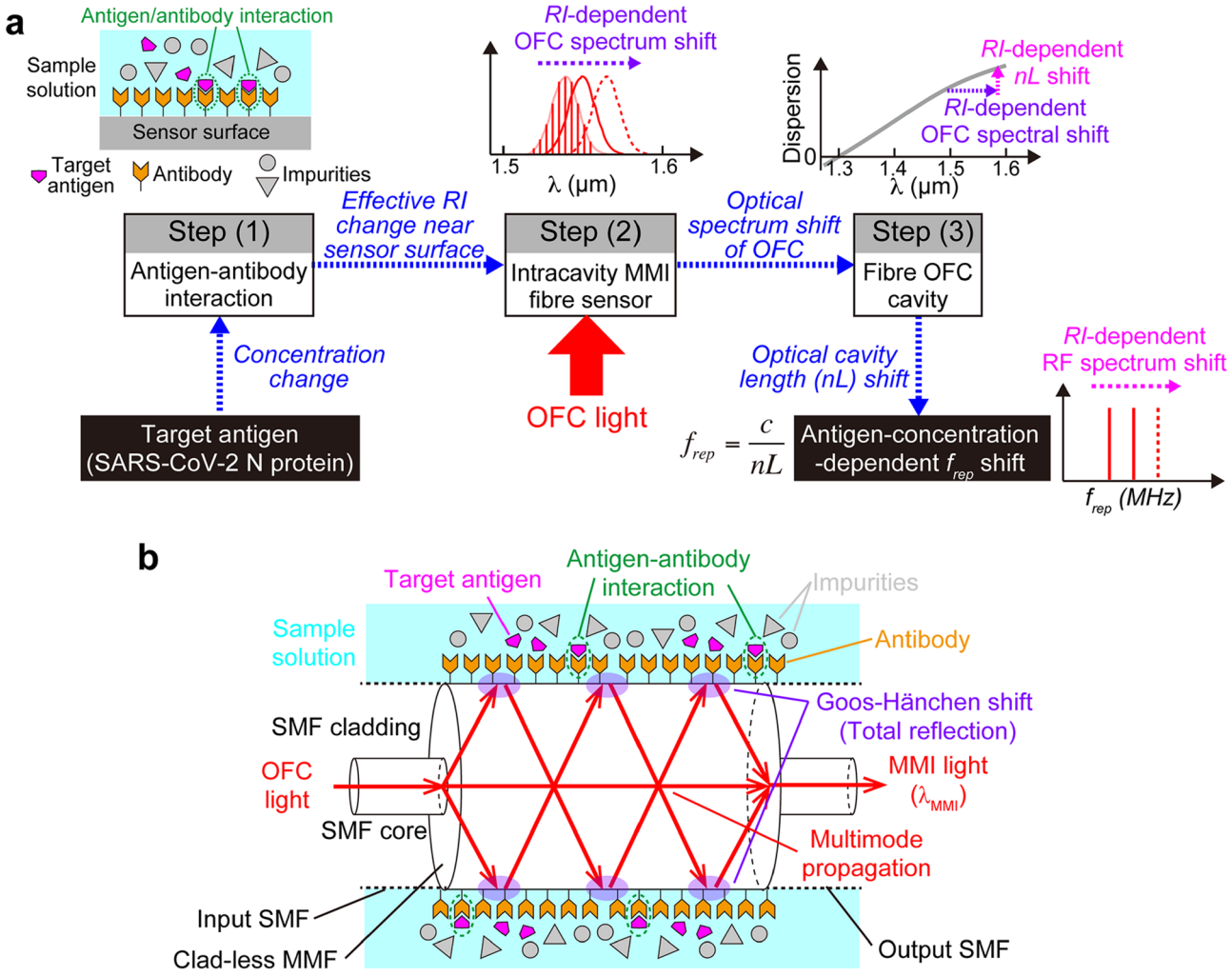

Figure 1. Principle of operation for the biosensing OFC. (**a**) Block diagram of the signal flow. The concentration of the target antigen is obtained according to the mode spacing f_{rep} of the OFC through three steps: Step (1) antigen–antibody interactions on the antibody-modified sensor surface, Step (2) RI-dependent optical spectrum shift of OFC provided by the intracavity MMI fiber sensor, and Step (3) photonic-to-RF conversion by the wavelength dispersion of the fiber cavity. (**b**) Schematic diagram of the intracavity MMI fiber sensor with antibody surface modification. The antigen–antibody interaction on the surface of the intracavity MMI fiber sensor is reflected by an effective RI change near the sensor surface, while the intracavity MMI fiber sensor functions as an RI-dependent variable-optical-bandpass filter via the MMI process. The combination of the antigen–antibody interaction with the MMI fiber sensor causes an antigen-concentration-dependent optical spectrum shift of OFC.

Importantly, the f_{rep} linewidth achieves down to below 1 Hz, which is smaller than f_{rep} shift expected due to the antigen concentration change.

Temperature drift in the single-comb configuration. We first evaluated the dependence of f_{rep} in a single sensing OFC on cavity temperature because the temperature disturbance to the fiber OFC cavity fluctuates f_{rep} via thermal expansion or shrinkage of nL. To this end, we measured the temporal drift in the f_{rep} of the single-comb configuration of sensing OFC under an uncontrolled cavity temperature, as shown in Fig. 2a, whose details are given in the Materials and Methods section. We set the center optical wavelength λ_{MMI} of 1556.6 nm and the frequency spacing f_{rep} of 31.7 MHz for stable mode-locked oscillation with the intracavity MMI fiber sensor. Pure water was used for a standard sample with a stable RI, and placed in a glass sample cell together with the MMI fiber sensor without the surface modification for RI sensing. The output light from the OFC was detected by a photodetector (PD), and f_{rep} was measured by an RF frequency counter synchronized to a rubidium frequency standard working in the RF band. Figure 2b shows the f_{rep} shift (δf_{rep}, blue line) when the cavity temperature (orange line) changed over a range of 1 °C. δf_{rep} represents the frequency deviation from the initial measurement value. The temporal behavior of δf_{rep} in synchronization with the cavity temperature indicated a temperature sensitivity of approximately − 400 Hz/°C. Thus, the cavity-temperature-dependent f_{rep} drift is considerably larger than the sample-concentration-dependent f_{rep} shift in biosensing (typically, a few to

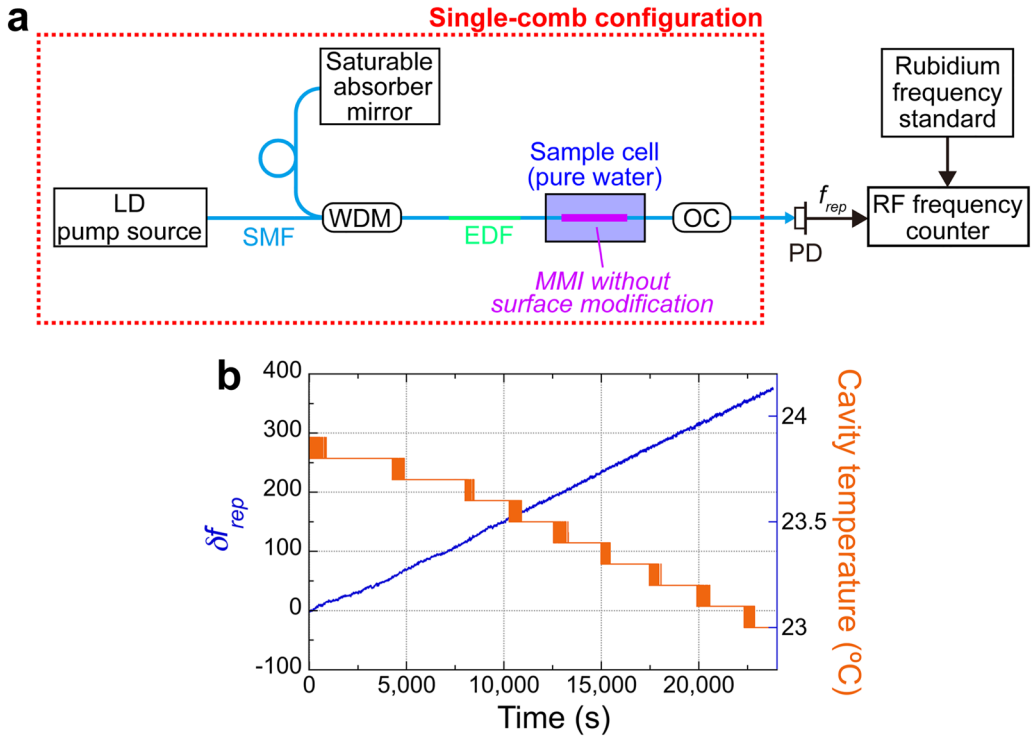

Figure 2. Basic performance of single-comb RI sensing of pure water with temperature drift. (**a**) Schematic drawing of the experimental setup. *LD* laser diode; *SMF* single-mode fiber; *WDM* wavelength-division-multiplexing coupler; *EDF* erbium-doped fiber; *MMI* multimode-interference fiber sensor; *OC* fiber output coupler; *PD* photodiode. Details of the single sensing OFC are given in the Materials and Methods section. (**b**) Temporal drift of the cavity temperature (orange line) and the corresponding f_{rep} shift (δf_{rep}, blue line). Pure water was used as the sample of RI sensing. δf_{rep} was calculated as the frequency deviation from the initial value of f_{rep}. The stepped-down behavior of the cavity temperature is due to the temperature resolution of the thermistor (= 0.1 °C) used for monitoring the cavity temperature. The cavity temperature sensitivity of the single sensing OFC was approximately − 400 Hz/°C.

a few tens Hz). Although the cavity temperature could be actively controlled within a range of 0.1 °C[34,36], it is still insufficient to suppress the cavity-temperature-dependent f_{rep} drift (= 400 Hz/°C × 0.1 °C = 40 Hz) below the sample-concentration-dependent f_{rep} shift. Thus, to further reduce the temperature drift, we applied a dual-comb configuration for active-dummy compensation of the temperature drift as described in the following subsection.

Active-dummy compensation of the temperature drift with the dual-comb configuration. A dual-comb configuration with an active sensing OFC with a frequency spacing of f_{rep1} and a dummy sensing OFC with a frequency spacing of f_{rep2} was adopted to compensate for the temperature drift. Figure 3a shows a schematic drawing of the dual-comb configuration, in which a pair of fiber OFC cavities were arranged in an aluminum box covered by insulated materials so that they were affected by similar temperature drifts [37]. In this configuration, although f_{rep1} and f_{rep2} fluctuate depending on the residual drift of cavity temperature via thermal expansion or shrinkage of nL, their drifts are similar because they experience the same thermal disturbances. Therefore, the frequency difference Δf_{rep} between f_{rep1} and f_{rep2} remains constant regardless of the temperature drift of f_{rep1} and f_{rep2}. Thus, when the active sensing OFC evaluates a sample solution in a certain temperature environment and the dummy sensing OFC evaluates a reference material in the same temperature environment, Δf_{rep} reflects the sample concentration without influence from temperature drift. In other words, a one-to-one correspondence between Δf_{rep} and the sample concentration is established independent of temperature drift. Figure 3b–d show the MMI and sample cell for dual-comb RI sensing of pure water, dual-comb RI sensing of glycerol solution, and dual-comb biosensing of the SARS-CoV-2 N protein antigen, respectively. Table 1 summarizes λ_{MMI}, f_{rep1}, f_{rep2}, Δf_{rep}, the MMI, and the sample cell used in the following three dual-comb sensing experiments; these values were selected for stable operation and better temperature compensation. A pair of output lights from the active and the dummy sensing OFCs is detected by a pair of photodetectors (PDs). Their frequency signals (= f_{rep1} and f_{rep2}) and a frequency difference between them (= $\Delta f_{rep} = f_{rep1} - f_{rep2}$) are measured by the RF frequency counter. Details of the dual-comb biosensing technique are given in the Materials and Methods section, together with details on the experimental and analytical methodology employed for all measurements.

The blue and green lines in Fig. 4 show the temporal shifts in f_{rep1} and f_{rep2}, namely, δf_{rep1} and δf_{rep2}, respectively, when pure water was used as a sample for both the active and dummy sensing OFCs without surface modification [see the second row in Table 1 and Fig. 3b]. δf_{rep1} and δf_{rep2} suffered from a frequency drift of over − 38 Hz,

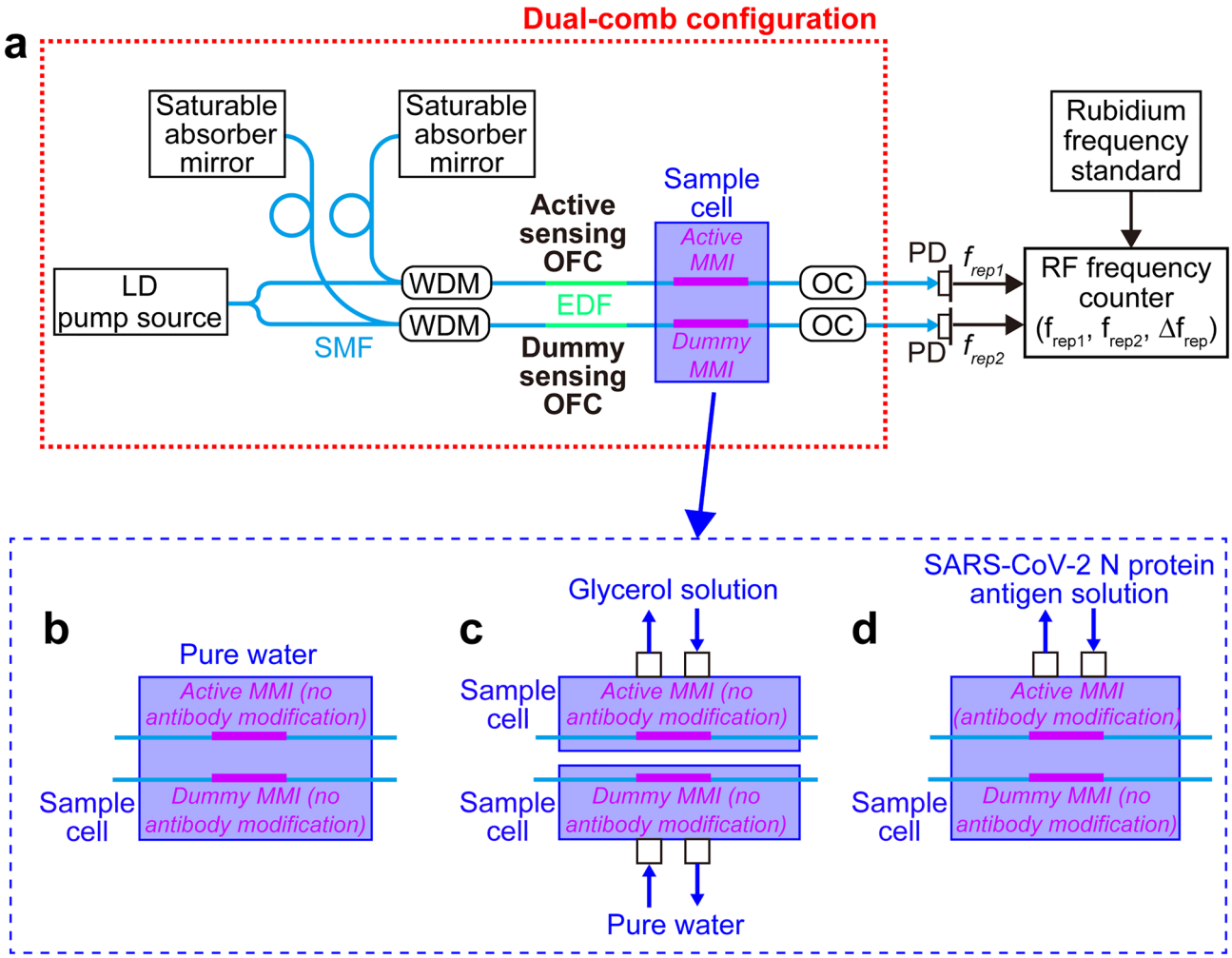

Figure 3. Experimental setup of dual-comb RI sensing and biosensing. (**a**) Schematic drawing of the whole experimental setup. *LD* laser diode; *SMFs* single-mode fibers; *OFCs* optical frequency combs; *WDMs* wavelength-division-multiplexing couplers; *EDF* erbium-doped fiber; *active MMI* intracavity multimode-interference fiber sensor for a target sample; *dummy MMI* intracavity multimode-interference fiber sensor for a reference sample; *OCs* fiber output couplers; *PDs* photodiodes. The active sensing OFC and dummy OFC operate at a center optical wavelength (λ_{MMI}) of 1556.6 nm. (**b**) Schematic drawing of the MMI sensor and sample cell for dual-comb RI sensing of pure water. (**c**) Schematic drawing of the MMI sensor and sample cell for dual-comb RI sensing of glycerol solution. (**d**) Schematic drawing of the MMI sensor and sample cell for dual-comb biosensing of the SARS-CoV-2 N protein antigen solution. Peristaltic pumps were used for sample exchange in the dual-comb RI sensing of glycerol solution and the dual-comb biosensing of the SARS-CoV-2 N protein antigen.

Experiments	λ_{MMI} (nm)	f_{rep1} (MHz)	f_{rep2} (MHz)	Δf_{rep} (kHz)	Active MMI	Dummy MMI	Sample cell
Dual-comb RI sensing of pure water	1556.6	31.7	32.5	− 851.9	No surface modification		Single [Fig. 3b]
Dual-comb RI sensing of glycerol solution	1556.6	31.7	32.5	− 851.9	No surface modification		Dual [Fig. 3c]
Dual-comb biosensing of SARS-CoV-2 N protein antigen	1556.6	29.6	29.7	− 88.6	Surface modification of antibody	No surface modification of antibody	Single [Fig. 3d]

Table 1. Experimental settings of dual-comb RI sensing and biosensing.

implying a temperature drift of 0.1 °C during the data acquisition from a temperature sensitivity of – 400 Hz/°C in Fig. 2b. However, importantly, δf_{rep1} and δf_{rep2} behaved almost the same in terms of drift. The resulting Δf_{rep} shift ($\delta\Delta f_{rep}$) was stable as shown by the red line in Fig. 4, in which the standard deviation of $\delta\Delta f_{rep}$ was 0.066 Hz at 10 s, 0.209 Hz at 100 s, and 0.177 Hz at 1000 s, respectively. These variations are equivalent to a temperature stability of 1.64×10^{-4} °C at 10 s, 5.23×10^{-4} °C at 100 s, and 4.42×10^{-4} °C at 1000 s, much better than that by the temperature controller of fiber OFC cavity.

We next tested active-dummy temperature compensation for RI sensing of a liquid sample different from the reference sample. For RI sensing, the active and dummy sensing OFCs have no surface modification in MMI [see the third row in Table 1 and Fig. 3c]. We used glycerol solutions consisting of glycerin and pure water at different ratios, corresponding to different RIs, as target samples in the active sensing OFC. This sample is easy to prepare and stable as it does not volatilize. We prepared six samples with different RIs [= 0 vol%, 1 vol%, 2 vol%, 3 vol%, 4 vol%, and 5 vol%, corresponding to 1.3165 RIU, 1.3179 RIU, 1.3193 RIU, 1.3207 RIU, 1.3222 RIU, and 1.3236 RIU; see color-highlighted zones in Fig. 5a,b] because their expected f_{rep} shift is comparable to the concentration-dependent f_{rep} shift caused by the SARS-CoV-2 N protein antigen. The RI of the sample was calculated from the volume ratio of water (RI = 1.3165 RIU at 1550 nm) and glycerin (RI = 1.4571 RIU at 1550 nm)[38]. While our experiments were conducted in volume ratio (vol%) of glycerin-water solutions, the correlation in the literature were provided in terms of weight ratio (wt%). To address this discrepancy, we performed a conversion between vol% and wt% by using the volume and density (= 1.26)[39] of 100% glycerin to calculate the corresponding weight, and then dividing it by the weight of water. This process yielded the weight ratio. Subsequently, we employed this weight ratio to calculate the RI value of each sample based on the RI values from the literature. We exchanged the sample by using a peristaltic pump [see grey zones in Fig. 5a,b]. Additionally, pure water (a 0 vol% glycerol solution, corresponding to 1.3165 RIU) was used as a reference sample in the dummy sensing OFC. To prevent the temperature of the pure water in the dummy sample cell from increasing during repeated measurements, the pure water sample was exchanged with a new pure water sample with another peristaltic pump when the target sample was exchanged with a new RI glycerol sample. The blue and green lines in Fig. 5a represent δf_{rep1} and δf_{rep2} as the concentration of the glycerol solution increased from 0 vol% to 5 vol%. δf_{rep2}, in the dummy sensing OFC, exhibited a slow drift with some rapid changes even though the RI of the pure water was constant. This slow drift is due to the temperature drift, too. Since rapid changes in δf_{rep2} were synchronized with the operation of the peristaltic pump, they are caused by disturbance from the water flow when the samples were exchanged. In contrast, δf_{rep1}, in the active sensing OFC, exhibited a combination of a step-like change with the sample RI and the slow drift shown by δf_{rep2} together with rapid changes. This combination of behavior in δf_{rep1} is detrimental to the RI sensing performance in the single sensing OFC configuration. The behavior of rapid changes caused by the peristaltic pump is different between δf_{rep1} and δf_{rep2} because the shape of the two separate sample cells is not identical, and the position of the MMI fiber sensors in those cells is not completely the same.

Figure 5b shows a sensorgram of $\delta\Delta f_{rep}$ calculated by subtracting the green line (δf_{rep2}) from the blue line (δf_{rep1}) in Fig. 5a. The temperature drift almost disappeared, and only the step-like change with the sample RI was present in $\delta\Delta f_{rep}$. The mean and the standard deviation of $\delta\Delta f_{rep}$ were 0.76 ± 0.19 Hz at 0 vol% or 1.3165 RIU, – 7.58 ± 0.24 Hz at 1 vol% or 1.3179 RIU, – 16.48 ± 0.52 Hz at 2 vol% or 1.3193 RIU, – 25.64 ± 0.53 Hz at 3 vol% or 1.3207 RIU, – 34.59 ± 0.31 Hz at 4 vol% or 1.3222 RIU, and – 43.12 ± 0.34 Hz at 5 vol% or 1.3236 RIU, as shown by red plots in Fig. 5c. From these values, we calculated a relation between the sample RI and $\delta\Delta f_{rep}$. The linear relation between the sample RI and $\delta\Delta f_{rep}$ was obtained with a correlation coefficient (R) of 0.9999. The good fitting result indicated that the dual-comb effect minimizes the effect of temperature drift. From the slope coefficient of the linear fitting (= – 6216 Hz/RIU) and the stability of $\delta\Delta f_{rep}$ (= 0.198 Hz at 10 s, 0.627 Hz at 100 s, and 0.531 Hz at 1000 s based on three times the standard deviation), the RI resolution was determined to be 3.19×10^{-5} RIU at 10 s, 1.01×10^{-4} RIU at 100 s, and 8.54×10^{-5} RIU at 1000 s. In RI sensing of a liquid sample (glycerol solutions) different from another liquid reference (pure water), difference of thermo-optic

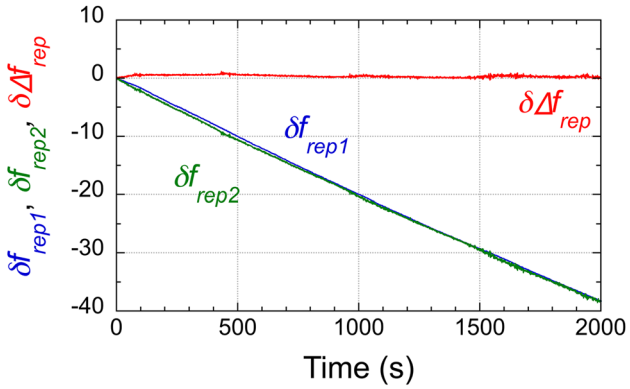

Figure 4. Basic performance of dual-comb RI sensing of pure water with temperature drift. Temporal drifts in δf_{rep1}, δf_{rep2}, and $\delta\Delta f_{rep}$ when pure water was used as a sample for the active and dummy RI-sensing OFCs [see the second row in Table 1 and Fig. 3b]. δf_{rep1}, δf_{rep2}, and $\delta\Delta f_{rep}$ were calculated as the frequency deviations from the initial values of f_{rep1}, f_{rep2}, and Δf_{rep}, respectively.

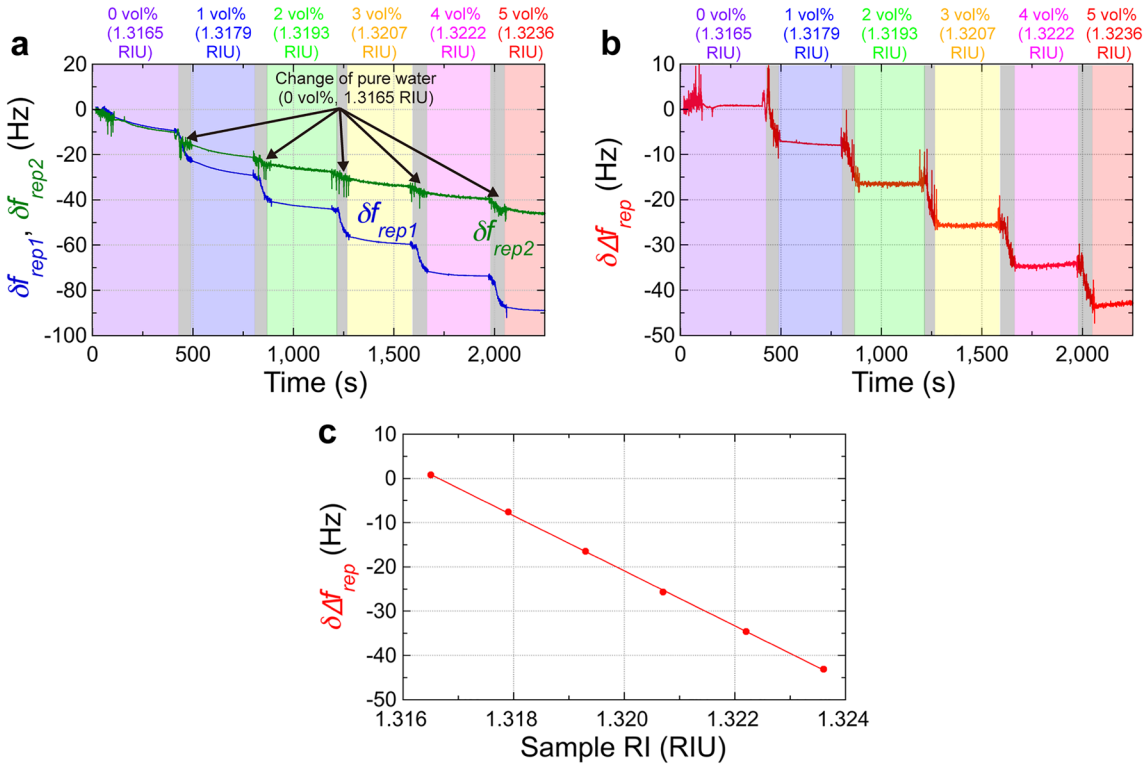

Figure 5. Temperature-drift-free dual-comb RI sensing of glycerol solution. (**a**) Sensorgrams of δf_{rep1} in the active sensing OFC and δf_{rep2} in the dummy sensing OFC. Glycerol solutions consisting of glycerin and pure water at different ratios were used as the target samples in the active sensing OFC; pure water was used as the reference sample in the dummy sensing OFC [see the third row in Table 1 and Fig. 3c]. Grey zones indicate the time period for sample exchange by peristaltic pumps. δf_{rep1} and δf_{rep2} were calculated as the frequency deviations from the initial values of f_{rep1} and f_{rep2}, respectively. (**b**) Sensorgram of $\delta\Delta f_{rep}$ with mixtures of glycerin and pure water at different ratios. $\delta\Delta f_{rep}$ was calculated as the frequency deviation from the initial value of Δf_{rep}. (**c**) Relationship between the sample RI and $\delta\Delta f_{rep}$.

effect between them may influence the effective RI and the temperature sensitivity because they have inherent thermo-optic coefficients (typically, 10^{-4} RIU/°C at 1550 nm)[40,41]. When their temperature is stable within a range of 0.1 °C, the drift of RI in the sample and the reference is estimated to be the order of 10^{-5} RIU. However, the temporal drift of thermo-optic coefficients will be common to each other if similar water solutions refer to the solutions used in the following measurements, and the active-dummy temperature compensation can work well. Therefore, the effect of different thermo-optic effects is negligible.

Rapid detection of SARS-CoV-2 N protein antigen. Antibody modification of the intracavity MMI fiber sensor creates a photonic RF biosensor for the detection of target antigens through antibody–antigen reactions because the RI-dependent f_{rep} shift is converted into an antigen-concentration-dependent f_{rep} shift [see Fig. 1a]. We confirmed the effectiveness of the active-dummy compensation with the dual-comb configuration in high-precision RI sensing demonstrated above. The resulting enhanced RI precision covers the effective RI change expected by the antigen–antibody interaction on the sensor surface, enabling us to apply these dual sensing OFCs for rapid, high-sensitive detection of viruses/pathogens and biological molecules.

The concept of the antigen–antibody interaction (in this case, a viral protein) was applied for the detection of SARS-CoV-2 protein with dual-comb biosensing. Among several proteins in SARS-CoV-2, we selected the N protein instead of the well-known and peculiar spike protein for antigen–antibody interactions. This is because the N protein functions to package the viral RNA genome within the viral envelope into a ribonucleoprotein complex and has benefits such as abundance, low probability of mutation, and relatively low molecular weight. We used a pair of a commercialized N protein antibody (Fapon Biotech Inc., Dongguan, Guangdong, China, FPZ0553) and a commercialized recombinant N protein antigen (Fapon Biotech Inc., Dongguan, Guangdong, China, FPZ0513) for antigen–antibody interactions in the intracavity MMI biosensor [see Fig. 1b]. Before performing the dual-comb biosensing, we evaluate the affinity of this pair by enzyme-linked immunosorbent assay (ELISA). Figure 6 shows a relation between antigen concentration and optical density at 450 nm, indicating a sensitivity within a range of 10 pM to 10 nM in ELISA. We made a surface modification of the MMI fiber sensor (material = SiO_2) with amino-terminated groups through a silane coupling reaction for a self-assembled monolayer (SAM) after surface cleaning and modifying by UV ozone. Then, the N protein antigen was immobilized on the amino-group-coated MMF fiber sensor surface to realize an active sensing OFC. Additionally, the

SAM without immobilized antibody was applied to the surface of the MMI fiber sensor for the dummy sensing OFC. The MMI fiber sensors with and without surface modification by the immobilized antibody were placed together in the same sample cell for the active and dummy sensing OFCs, respectively [see the last row in Table 1 and Fig. 3d]. Solution samples of the N protein antigen in phosphate-buffered saline (PBS) at different molar concentrations were consecutively introduced into the sample cell with a peristaltic pump. The N protein antigen–antibody interaction could only occur on the sensor surface of the active sensing OFC because that of the dummy sensing OFC did not include immobilized antibodies. Thus, the dummy sensing OFC was used for the compensation of temperature drift assuming that non-specific adsorption did not occur on the sensor surface of the dummy sensing OFC.

Figure 7a shows the sensorgram of δf_{rep1} and δf_{rep2} as the molar concentration of the antigen/PBS solution increased from 1 aM (blue zone), 1 fM (green zone), 1 pM (yellow zone), and 1 nM (red zone) after starting with pure PBS (purple zone). We here selected the considerably wide range of molar concentrations for the initial evaluation of basic performance in dual-comb biosensing of SARS-CoV-2 N protein antigen. The precise evaluation focused within the clinically-relevant range of SARS-CoV-2 N protein antigen will be the future work. The time period for data acquisition [see color-highlighted zones in Fig. 7a] was set to 10 min. In the grey zones (time period = 8 min), we performed the following three steps: (1) we introduced the antigen/PBS solution into the sample cell with the peristaltic pump (1.5 min), (2) we waited for the antigen–antibody interaction to be completed (5 min), and (3) we rinsed the sensor surface with PBS to flush the accumulated N protein antigen that did not interact with the antibodies away (1.5 min). When the antigen was washed with the PBS buffer after being added and waited, the sensor signal reflects the amount of the antigen adsorbed on the sensor surface after desorption. However, the step-like change in δf_{rep1} with the antigen concentration was completely overshadowed by the background temperature drift. So, we next calculated the frequency difference ($\delta\Delta f_{rep}$) between δf_{rep1} and δf_{rep2} to eliminate the influence of temperature drift as described in the previous subsection. Figure 7b shows the sensorgram of $\delta\Delta f_{rep}$. Focusing on the zones highlighted in colors other than grey, a slightly dull stepped change in $\delta\Delta f_{rep}$ dependent on the molar concentration was observed, although a small drift in $\delta\Delta f_{rep}$ within the range of a few Hz remained at each molar concentration. To evaluate the validity of this behavior in the sensorgram, we calculated the mean and the standard deviation of $\delta\Delta f_{rep}$ at each molar concentration (each color zone other than grey zones): − 1.42 ± 1.00 Hz at 1 aM, − 8.82 ± 0.57 Hz at 1 fM, − 24.29 ± 0.36 Hz at 1 pM, and − 27.52 ± 1.08 Hz at 1 nM, respectively. They are indicated as red circles and corresponding error bars in Fig. 7c. The negative slope was consistent with the RI dependence of $\delta\Delta f_{rep}$ [see the red line plotted in Fig. 5c] because the progression of the antigen–antibody reaction increases the effective RI near the MMI fiber sensor and hence decreases f_{rep}[42]. In this way, we demonstrated the potential for rapid detection of the SARS-CoV-2 N protein antigen within this range of molar concentrations.

Discussion

To achieve the rapid, high-sensitivity detection of biomolecules, we developed dual-comb biosensing. Benefiting from the photonic-to-RF conversion in OFC, the enhanced sensitivity by the intracavity biosensor, and the active-dummy dual-comb compensation of temperature drift, the detection of the SARS-CoV-2 N protein antigen with a molar concentration from 1 aM to 1 nM was demonstrated in the measurement time of 10 min.

We first perform the quantitative analysis of the result shown in Fig. 7c. The antigen–antibody reaction is represented by a sigmoidal curve, often used when discussing the biosensor performance[43]; thus, the sigmoidal curve was applied to the experimental data to evaluate the ability of dual-comb biosensing to sense the SARS-CoV-2 N protein antigen. The sigmoidal function of Hill plot is given by

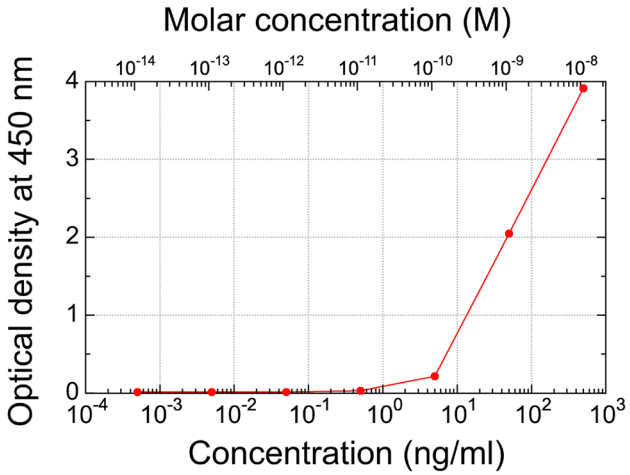

Figure 6. Affinity test between a commercialized antibody (FPZ0553, Fapon Biotech Inc.) and a commercialized antigen (FPZ0513, Fapon Biotech Inc.) for SARS-CoV-2 N protein by ELISA.

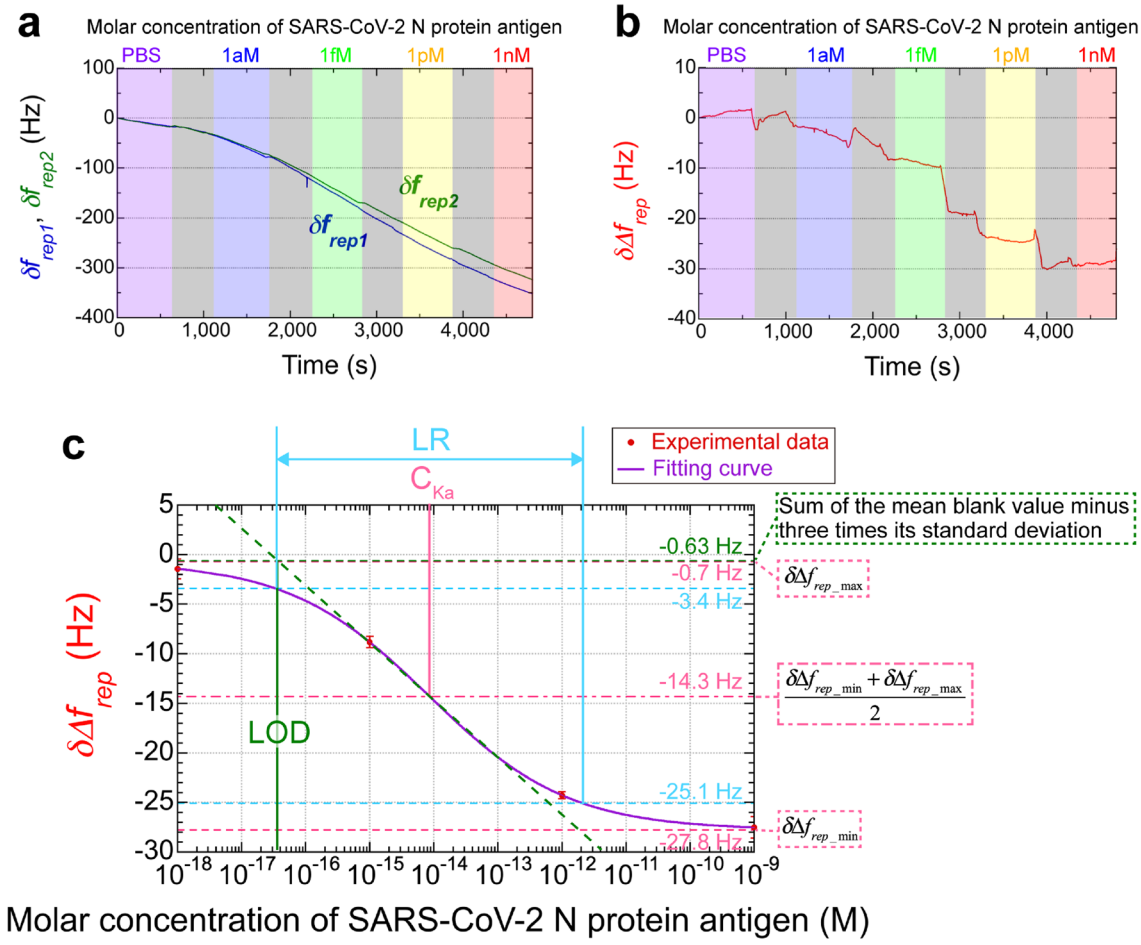

Figure 7. Rapid, high-sensitivity, dual-comb biosensing of the SARS-CoV-2 N protein antigen. (**a**) Sensorgram of δf_{rep1} and δf_{rep2} with respect to different molar concentrations of the SARS-CoV-2 N protein antigen. δf_{rep1} and δf_{rep2} were calculated as the frequency deviations from the initial values of f_{rep1} and f_{rep2}, which were measured for the active biosensing OFC with immobilized antibody and the dummy OFC without immobilized antibody, respectively [see the last row in Table 1 and Fig. 3d]. Grey zones indicate the time period for sample exchange. (**b**) Sensorgram of $\delta\Delta f_{rep}$ with respect to different molar concentrations of the SARS-CoV-2 N protein antigen. $\delta\Delta f_{rep}$ was calculated as the frequency deviation from the initial value of Δf_{rep}. (**c**) Relationship between the antigen molar concentration and $\delta\Delta f_{rep}$. Red circles show experimental data obtained from the sensorgram of $\delta\Delta f_{rep}$. The purple line shows the fitting curve for the sigmoidal function of the Hill plot.

$$\delta\Delta f_{rep} = \delta\Delta f_{rep\_min} + \frac{\delta\Delta f_{rep\_max} - \delta\Delta f_{rep\_min}}{1 + \left(\frac{[C]}{[C_{Ka}]}\right)^{n}}, \tag{2}$$

where $\delta\Delta f_{rep\_max}$ and $\delta\Delta f_{rep\_min}$ are the maximum and minimum of $\delta\Delta f_{rep}$ within a range of 1 aM to 1 nM, n is the Hill coefficient, C is the concentration of the antigen, and C_{Ka} is the dissociation constant. The purple line in Fig. 7c represents the sigmoidal fit of the experimental data. Unfortunately, in this fitting analysis, as the number of unknown parameters of the sigmoidal curve (N = 4, $\delta\Delta f_{rep\_min}$, $\delta\Delta f_{rep\_max}$, C_{Ka}, and n) is equal to the number of input data (N = 4, concentrations of 1 aM, 1 fM, 1 pM, and 1 nM), the degrees of freedom for the fitting are zero. In other words, results of this fit may be unreliable. The primary focus here is to roughly calculate performance parameters for biosensing using experimental data within specific concentration ranges. Based on the zero-degree-of-freedom fitting results, we will then proceed to engage in the following discussions. Addressing the issue of the zero-degree-of-freedom fitting results through detailed quantitative analysis will be part of our future work. From the curve fitting analysis of experimental plots with Eq. 2, we determined the following four parameters: $\delta\Delta f_{rep\_min} = -27.8$ Hz, $\delta\Delta f_{rep\_max} = -0.7$ Hz, $C_{Ka} = 8.4$ fM, and $n = 0.40$. C_{Ka} [see the pink solid line in Fig. 7c] is corresponding to the molar concentration at the middle [= −14.3 Hz, see pink the dashdotted line in Fig. 7c] between $\delta\Delta f_{rep\_max}$ and $\delta\Delta f_{rep\_min}$ [see pink dashed lines in Fig. 7c]. When the linear range (LR) was defined as the molar concentration at 10 ~ 90% (= −3.4 ~ −25.1 Hz) of the dynamic signal range of $\delta\Delta f_{rep\_max}$ to $\delta\Delta f_{rep\_min}$ [see blue dashed lines in Fig. 7c][43], it was determined to be 34 aM ~ 2.1 pM [see blue solid lines in Fig. 7c]. Since the mean $\delta\Delta f_{rep}$ value (= 0.93 Hz) minus three times its standard deviation (= 0.52 Hz) of the blank sample (PBS)

was − 0.63 Hz [see the purple zone in Fig. 7b], the LOD was calculated to be 37 aM from the crossover point [see the green solid line in Fig. 7c] between it and the linear approximation given by the Hill coefficient n (= 0.40).

We next compare the performance between the dual-comb biosensing and other biosensors when they are applied for biosensing of SARS-CoV-2 protein. While SPR benefits from the rapid analysis, its analytical sensitivity remains in LR of 2 ~ 1000 ng/mL with LOD of 1.02 pM[44]. The plasmonic enhancement by large gold nanoparticle decreases the LOD of SPR down to 85 fM or 4 pg/ml[14]. Also, the dual-functional plasmonic biosensor combining the plasmonic photothermal effect and localized SPR indicates LOD of 0.22 pM and LR of 0.1 pM ~ 1 μM[45]. In addition to these optical biosensors, colorimetric assay can be used for the detection of SARS-CoV-2 with a LOD of 0.18 ng/μL and a LR of 0.2 ~ 3 ng/μL within 10 min[46]. Dual-comb biosensing of SARS-CoV-2 N protein antigen achieves a LOD of 37 aM and a LR of 34 aM ~ 2.1 pM within 10 min in a simple matrix of PBS buffer that contains no interfering proteins, enzymes, and biomolecules. The above LOD and LR given in molar concentration correspond to concentrations of 1.7 fg/mL and 1.6 fg/mL ~ 99 pg/mL based on the molecular weight of the SARS-CoV-2 N protein antigen (= 47 kDa). When using complex matrices such as blood plasma or serum in place of PBS, testing time may increase depending on analyte diffusion and/or binding kinetics; still, it's within a range of 10 min. Table 2 summarizes the comparison of those biosensors for SARS-CoV-2 protein. In this way, the dual-comb biosensing greatly outperforms other biosensors in terms of LOD and LR.

Since we demonstrated the dual-comb biosensing of SARS-CoV-2 N protein antigen using highly purified, synthetic laboratory samples, the demonstrated results could not guarantee about the real specificity in the detection, which is another important performance of biosensing. For a real assessment of the biosensing performance including the specificity, a sample of complex matrices such as blood plasma or serum should be evaluated. In this case, non-specific adsorption of other proteins on the sensor surface spoils the specificity of dual-comb biosensing. We have to make special surface modifications designed to avoid non-specific adsorption in the active and the dummy sensing OFCs together with a specific antibody of SARS-CoV-2 N protein enhancing the specificity. Use of nucleic acids (DNA probe)[47], in place of antibody–antigen, as biomolecular interaction also enables us to enhance the specificity of dual-comb biosensing largely. Work is in progress to enhance the specificity of the dual-comb biosensing by these approaches.

We finally discuss the potential for dual-comb biosensing to be used for the detection of other biomolecules of interest. The achieved C_{Ka} (= 8.4 fM) is considerably low, enabling its easy use for a wide variety of biosensing applications. For example, it has an option for early detection and quantification of cancer cells from a droplet of blood or other body fluids by detecting a sugar chain specifically expressed on the surface of cancer cells. Such liquid biopsy[48] will be a powerful tool for detection of important biomarkers, such as proteins or RNA, in addition to cancer cells. Furthermore, if the molecular identification in biosensing is implemented by DNA probes in place of antigen–antibody reactions, it enables biosensing of exosomes via miRNA. As exosomes play an important role for intercellular communication, the biosensing of them is expected to make a great contribution to the diagnosis (marker) and treatment (drug delivery) of diseases such as cancer and Alzheimer's disease.

Conclusion

We have demonstrated the dual-comb biosensing for rapid, high-sensitivity detection of biomolecules. To the best of our knowledge, this is the first application of an OFC as a biosensor itself. The integration of photonic-to-RF conversion, an intracavity sensor, and active-dummy dual-comb compensation in the OFC enables detection of the SARS-CoV-2 N protein antigen with an LOD of 37 aM in a measurement time of 10 min. The current COVID-19 pandemic may diminish in the near future; however, we are always at risk of facing another emerging and re-emerging infectious disease again. As dual-comb biosensing can be used for other viruses through selection of the antigen–antibody reaction or other molecular identifications, it will be important as a proactive measure against unknown infectious diseases. Simultaneous achievement of high sensitivity and rapid measurement by the dual-comb biosensing will greatly enhance the applicability of biosensors to viruses, biomarkers, environmental hormones, and so on.

Materials and methods

MMI fiber sensor. Figure 1b shows a schematic diagram of the intracavity MMI fiber sensor with antibody surface modification. When the surface of the fiber sensor is not modified with an antibody, the MMI fiber sensor functions as an RI sensor. The MMI fiber sensor is composed of a clad-less multimode fiber (MMF; Thorlabs Inc., Newton, NJ, USA, FG125LA, core diameter = 125 μm, fiber length = 58.94 mm) with a pair of single-mode fibers (SMFs) at both ends (Corning Inc., Corning, NY, USA, SMF28e + , core diameter = 8.2 μm,

Method	Limit of detection	Linear range	Time	Matrix	Target	References
SPR	1.02 pM	2 ~ 1000 ng/mL	–	PBS containing 0.1% Tween 20	N protein antigen	44
Nanoplasmonic-enhanced SPR	85 fM (4 pg/ml)	85 fM ~ 2 pM	5 min	PBS	N protein antigen	14
Dual-functional plasmonic biosensor	0.22 pM	0.1 pM ~ 1 μM	–	Nuclease-free water	Nucleic acid	45
Colorimetric assay	0.18 ng/μL	0.2 ~ 3 ng/μL	10 min	RNase H reaction buffer	N phosphoprotein gene	46
Dual-comb biosensing	37 aM (1.7 fg/ml)	34 aM ~ 2.1 pM (1.6 fg/ml ~ 99 pg/ml)	10 min	PBS	N protein antigen	–

Table 2. Comparison of testing methods for SARS-CoV-2.

cladding diameter = 125 μm, fiber length = 150 mm)[34–36]. Only the exposed core of the clad-less MMF functions as a sensing part. The OFC light passing through the input SMF is diffracted at the entrance face of the clad-less MMF and then undergoes repeated total internal reflection at the boundary between the clad-less MMF core surface and the sample solution. Only the OFC modes satisfying the MMI wavelength λ_{MMI} can exit through the clad-less MMF and then be transmitted through the output SMF. λ_{MMI} is given by

$$\lambda_{MMI} = \frac{n_{MMF} m_{MMI}}{L_{MMF}} [D(n_{sam})]^2, \tag{3}$$

where L_{MMF} and n_{MMF} are the geometrical length and RI of the clad-less MMF, m_{MMI} is the order of the MMI, n_{sam} is the RI near the clad-less MMF core surface (namely, sample RI), and $D(n_{sam})$ is the effective core diameter of the clad-less MMF. Since $D(n_{sam})$ is influenced by the Goos-Hänchen shift on the core surface of the clad-less MMF, λ_{MMI} is a function of the sample RI near the sensor surface. The intracavity MMI fiber sensor in this study functions as an RI-dependent optical bandpass filter tunable around λ_{MMI} (= 1556.6 nm) with constructive interference at $m = 4$. This λ_{MMI} was selected to match a spectral peak of the fiber OFC, suppressing the power loss. The RI-dependent λ_{MMI} shift of the OFC is converted into an RI-dependent f_{rep} shift via the wavelength dispersion of the cavity fiber [see Fig. 1a]. Furthermore, if the surface of the MMI fiber sensor is modified with a virus antibody, then the RI-dependent f_{rep} shift is converted into a virus-antigen-concentration-dependent f_{rep} shift through antibody–antigen reactions. In other words, the intracavity MMI fiber sensor with antibody surface modification enables a photonic RF biosensor for viruses.

Single-comb configuration of the sensing OFC. We used a linear fiber cavity mode-locked by a saturable absorber mirror for easy, stable, mode-locked oscillation and compact size [see Fig. 2a]. The linear cavity includes a 2.6-m-long SMF (SMF; Corning Inc., Corning, NY, USA, SMF28e+, dispersion at 1550 nm = 17 ps km^{-1} nm^{-1}), a 0.6-m-long erbium-doped fiber (EDF; nLIGHT Inc., Camas, WA, USA, LIEKKI ER30-4/125, dispersion at 1550 nm = − 22.75 ps km^{-1} nm^{-1}), a saturable absorber mirror (BATOP GmbH, Jena, Germany, SAM-1550–55-2 ps-1.3b-0, high reflection band = 1480–1640 nm, absorbance = 55%, modulation depth = 2.4%, relaxation time constant = ~ 2 ps, size = 1.3 mm width, 1.3 mm height, 0.4 mm thickness), a wavelength-division-multiplexing coupler (WDM; AFR Ltd., Zhuhai, China, WDM-1–9855-N-B-1-F), a pumping laser diode (LD pump source; Thorlabs Inc., Newton, NJ, USA, BL976-PAG700, wavelength = 976 nm, power = 700 mW), a 90:10 fiber output coupler (OC; AFR Ltd., Zhuhai, China, PMOFM-55–2-B-Q-F-90), and an intracavity MMI fiber sensor (MMI). The total dispersion of the fiber cavity was set to − 0.12 pm/s^2 for stable operation. The fiber cavity was placed in an aluminum box, and its temperature was not actively controlled. The light output of the sensing OFC was detected by a photodetector (PD; Thorlabs Inc., Newton, NJ, USA, PDA05CF2, wavelength = 800 ~ 1700 nm, frequency bandwidth = 150 MHz), and the resulting frequency signal of f_{rep} was measured by an RF frequency counter (Keysight Technologies, Santa Rosa, CA, USA, 53230A, frequency resolution = 12 digit s^{-1}) synchronized to a rubidium frequency standard (Stanford Research Systems Inc., Sunnyvale, CA, USA, FS725, frequency = 10 MHz, accuracy = 5×10^{-11}, and instability = 2×10^{-11} at 1 s).

Dual-comb configuration of active and dummy sensing OFCs. We used a pair of linear-cavity sensing OFCs (frequency spacing = f_{rep1} and f_{rep2}, frequency difference between them = $\Delta f_{rep} = f_{rep1} - f_{rep2}$) for the active sensing OFC and the dummy sensing OFC in the dual-comb configuration [see Fig. 3a]. The configuration of each linear cavity was similar to that in Fig. 2a. The output light of the LD pump source was split into two beams and used for these two OFCs, which eliminates the influence of power drifts in the LD pump source through common-mode behavior. These OFC fiber cavities were enclosed in an aluminum box. Specification of the active and dummy sensing OFCs are shown in Table 1. The light output of the dual OFCs was detected by a pair of PDs, and the resulting frequency signals of f_{rep1}, f_{rep2} and Δf_{rep} were measured through a combination of an RF frequency counter and a rubidium frequency standard.

SARS-CoV-2 nucleocapsid protein antigen. The recombinant SARS-CoV-2 nucleocapsid protein, expressed in Escherichia coli, was used as an antigen. The molecular weight of 47 kDa was calculated based on the amino acid sequence of 419 residues using the molecular weight calculation tool provided by Expasy[49]. We further validated this by referring to literature that documented the utilization of a similar N capsid protein[50,51]. The slight variation in molecular weight compared to previous literature is thought to be attributed to differences in the His-Tag sequence and/or uncertainties in band reading on SDS-PAGE.

Enzyme-linked immunosorbent assay (ELISA). Recombinant SARS-CoV-2 nucleocapsid protein antigen (FPZ0513, 2 μg/ml) in phosphate-buffered saline (PBS) was added to 96-well EIA/RIA plates (Corning Inc., Corning, NY, U.S.) and incubated overnight at room temperature. Non-specific sites were blocked with Blocking One (Nacalai Tesque, Inc., Kyoto, Japan). After the plates were washed, diluted anti-SARS-CoV-2 nucleocapsid monoclonal antibody (FPZ0553) was added. After 1 h incubation at room temperature and washing the plates, goat anti-mouse IgG, (H + L) horseradish peroxidase conjugated (Invitrogen) was used as the secondary antibody. After washing the plates two times, TMB substrate solution (Invitrogen, Thermo Fisher Scientific Inc., Waltham, MA, U.S.) was added. The OD at 450 nm for each well was measured using a SpectraMax ABS microplate reader (Molecular Devices, San Jose, CA, U.S.).

Antibody modification of the MMI fiber sensor. A schematic diagram of the intracavity MMI fiber sensor with antibody surface modification is shown in Fig. 1b. First, a UV ozone cleaner (Sun Energy Corp.,

Minoo, Osaka, Japan, SKB1101N-01) was applied to the MMI fiber sensor for 30 min to remove any organic compounds on the surface of the clad-less MMF and modify the resulting surface with hydroxy groups. Second, the surface of the clad-less MMF was modified with amino-terminated groups through a silane coupling reaction using 1% (v/v) 3-aminopropyltriethoxysilane (APTES) in ethanol for 1 h, followed by washing with ultrapure water and drying at 110 °C for 10 min. Third, for the antibody immobilization step by amide bonding, a dehydro-condensation reaction was used, which is a one-step reaction with higher reaction efficiency even in buffer solution, instead of the conventional method using carbodiimide activation[52]. The monoclonal antibody specific for the N protein antigen was immobilized on the amino-group-coated MMF core by a dehydration-condensation reaction using 10 mM 4-(4,6-dimethoxy-1,3,5-triazin-2-yl)-4-methylmorpholinium chloride (DMTMM) in PBS buffer (pH 7.4)[53].

Data analysis. The frequency spacings of the OFCs (f_{rep}, f_{rep1}, and f_{rep2}) were continuously acquired by an RF frequency counter with a gate time of 100 ms and a sampling interval of 2.8 s. The frequency difference Δf_{rep} between f_{rep1} and f_{rep2} was calculated from acquired f_{rep1} and f_{rep2}. Finally, δf_{rep}, δf_{rep1}, δf_{rep2}, and $\delta\Delta f_{rep}$ were calculated as the frequency deviations from the initial values of f_{rep}, f_{rep1}, f_{rep2}, and Δf_{rep}, respectively. In the dual-comb biosensing of SARS-CoV-2 N protein antigen, we calculated the 99.9% confidence interval for the first 100 data of the $\delta\Delta f_{rep}$ sensorgram measured in the PBS, and then used it as a criterion of rejection test to judge whether $\delta\Delta f_{rep}$ value acquired at each molar concentration is considered as a measurement error.

Data availability

Data underlying the results presented in this paper are not publicly available at this time but may be obtained from Takeshi Yasui upon reasonable request.

Received: 9 April 2023; Accepted: 26 August 2023
Published online: 26 September 2023

References

1. Suo, T. *et al.* ddPCR: A more accurate tool for SARS-CoV-2 detection in low viral load specimens. *Emerg. Microbes Infect.* **9**(1), 1259–1268 (2020).
2. Panpradist, N. *et al.* Simpler and faster Covid-19 testing: Strategies to streamline SARS-CoV-2 molecular assays. *EBioMedicine* **64**, 103236 (2021).
3. Oranger, A. *et al.* Accurate detection and quantification of SARS-CoV-2 genomic and subgenomic mRNAs by ddPCR and meta-transcriptomics analysis. *Commun. Biol.* **4**(1), 1215 (2021).
4. Borisov, S. M. & Wolfbeis, O. S. Optical biosensors. *Chem. Rev.* **108**(2), 423–461 (2008).
5. Damborský, P., Švitel, J. & Katrlík, J. Optical biosensors. *Essays Biochem.* **60**(1), 91–100 (2016).
6. Homola, J., Yee, S. S. & Gauglitz, G. Surface plasmon resonance sensors: Review. *Sens. Actuators B* **54**(1–2), 3–15 (1999).
7. Pattnaik, P. Surface plasmon resonance. *Appl. Biochem. Biotechnol.* **126**(2), 079–092 (2005).
8. Liu, Y. & Huang, C. Z. One-step conjugation chemistry of DNA with highly scattered silver nanoparticles for sandwich detection of DNA. *Analyst* **137**(15), 3434–3436 (2012).
9. Sharma, P. K. *et al.* Surface plasmon resonance sensing of Ebola virus: A biological threat. *Anal. Bioanal. Chem.* **412**, 4101–4112 (2020).
10. Ashiba, H. *et al.* Detection of norovirus virus-like particles using a surface plasmon resonance-assisted fluoroimmunosensor optimized for quantum dot fluorescent labels. *Biosens. Bioelectron.* **93**, 260–266 (2017).
11. Bai, H., Wang, R., Hargis, B., Lu, H. & Li, Y. A SPR aptasensor for detection of avian influenza virus H5N1. *Sensors* **12**(9), 12506–12518 (2012).
12. Djaileb, A., Charron, B., Jodaylami, M. H., Thibault, V., Coutu, J., Stevenson, K., Forest, S., Live, L. S., Boudreau, D., Pelletier, J. N. & Masson, J.-F. A rapid and quantitative serum test for SARS-CoV-2 antibodies with portable surface plasmon resonance sensing. ChemRxiv (2020).
13. Moznuzzaman, M., Khan, I. & Islam, M. R. Nano-layered surface plasmon resonance-based highly sensitive biosensor for virus detection: A theoretical approach to detect SARS-CoV-2. *AIP Adv.* **11**(6), 065023 (2021).
14. Yano, T. *et al.* Ultrasensitive detection of SARS-CoV-2 nucleocapsid protein using large gold nanoparticle-enhanced surface plasmon resonance. *Sci. Rep.* **12**(1), 1–8 (2022).
15. Bian, S. *et al.* Development and validation of an optical biosensor for rapid monitoring of adalimumab in serum of patients with Crohn's disease. *Drug Test. Anal.* **10**(3), 592–596 (2018).
16. Singh, M. *et al.* Noncovalently functionalized monolayer graphene for sensitivity enhancement of surface plasmon resonance immunosensors. *J. Am. Chem. Soc.* **137**(8), 2800–2803 (2015).
17. Pollet, J., Janssen, K. P. F., Knez, K. & Lammertyn, J. Real-time monitoring of solid-phase PCR using fiber-optic SPR. *Small* **7**(8), 1003–1006 (2011).
18. Daems, D., Knez, K., Delport, F., Spasic, D. & Lammertyn, J. Real-time PCR melting analysis with fiber optic SPR enables multiplex DNA identification of bacteria. *Analyst* **141**(6), 1906–1911 (2016).
19. Malachovská, V. *et al.* Fiber-optic SPR immunosensors tailored to target epithelial cells through membrane receptors. *Anal. Chem.* **87**(12), 5957–5965 (2015).
20. Leonard, P., Hearty, S., Quinn, J. & O'Kennedy, R. A generic approach for the detection of whole Listeria monocytogenes cells in contaminated samples using surface plasmon resonance. *Biosens. Bioelectron.* **19**(10), 1331–1335 (2004).
21. Cha, H. *et al.* Surface-enhanced Raman scattering-based immunoassay for severe acute respiratory syndrome coronavirus 2. *Biosens. Bioelectron.* **202**, 114008 (2022).
22. Taitt, C. R., Anderson, G. P. & Ligler, F. S. Evanescent wave fluorescence biosensors: Advances of the last decade. *Biosens. Bioelectron.* **76**, 103–112 (2016).
23. Lochhead, M. J. *et al.* Rapid multiplexed immunoassay for simultaneous serodiagnosis of HIV-1 and coinfections. *J. Clin. Microbiol.* **49**(10), 3584–3590 (2011).
24. Dinish, U. S. *et al.* Highly sensitive SERS detection of cancer proteins in low sample volume using hollow core photonic crystal fiber. *Biosens. Bioelectron.* **33**(1), 293–298 (2012).
25. Srivastava, S. K. *et al.* SERS biosensor using metallic nano-sculptured thin films for the detection of endocrine disrupting compound biomarker vitellogenin. *Small* **10**(17), 3579–3587 (2014).

26. Udem, T., Reichert, J., Holzwarth, R. & Hänsch, T. W. Accurate measurement of large optical frequency differences with a mode-locked laser. *Opt. Lett.* **24**(13), 881–883 (1999).
27. Niering, M. *et al.* Measurement of the hydrogen 1S–2S transition frequency by phase coherent comparison with a microwave cesium fountain clock. *Phys. Rev. Lett.* **84**(24), 5496–5499 (2000).
28. Jones, D. J. *et al.* Carrier-envelope phase control of femtosecond mode-locked lasers and direct optical frequency synthesis. *Science* **288**(5466), 635–639 (2000).
29. Udem, T., Holzwarth, R. & Hänsch, T. W. Optical frequency metrology. *Nature* **416**(6877), 233–237 (2002).
30. Wang, S. *et al.* Passively mode-locked fiber laser sensor for acoustic pressure sensing. *J. Mod. Opt.* **60**(21), 1892–1897 (2013).
31. Minamikawa, T. *et al.* Strain sensing based on strain to radio-frequency conversion of optical frequency comb. *Opt. Express* **26**(8), 9484–9491 (2018).
32. Taue, S., Matsumoto, Y., Fukano, H. & Tsuruta, K. Experimental analysis of optical fiber multimode interference structure and its application to refractive index measurement. *Jpn. J. Appl. Phys.* **51**(4S), 04DG14 (2012).
33. Fukano, H., Watanabe, D. & Taue, S. Sensitivity characteristics of multimode-interference optical-fiber temperature-sensor with solid cladding material. *IEEE Sens. J.* **16**(24), 8921–8927 (2016).
34. Oe, R. *et al.* Refractive-index-sensing optical comb based on photonic radio-frequency conversion with intracavity multi-mode interference fiber sensor. *Opt. Express* **26**(15), 19694–19706 (2018).
35. Oe, R. *et al.* Refractive index sensing with temperature compensation by a multimode-interference fiber-based optical frequency comb sensing cavity. *Opt. Express* **27**(15), 21463–21476 (2019).
36. Oe, R. *et al.* Improvement of dynamic range and repeatability in a refractive-index-sensing optical comb by combining saturable-absorber-mirror mode-locking with an intracavity multimode interference fiber sensor. *Jpn. J. Appl. Phys.* **58**(6), 060912 (2019).
37. Nakajima, Y., Kusumi, Y. & Minoshima, K. Mechanical sharing dual-comb fiber laser based on an all-polarization-maintaining cavity configuration. *Opt. Lett.* **46**(21), 5401–5404 (2021).
38. Saunders, J. E., Sanders, C., Chen, H. & Loock, H.-P. Refractive indices of common solvents and solutions at 1550 nm. *Appl. Opt.* **55**(4), 947–953 (2016).
39. Glycerine Producers' Association. *Physical properties of glycerine and its solutions.* Glycerine Producers' Association (1963).
40. Kamikawachi, R. C. *et al.* Determination of thermo-optic coefficient in liquids with fiber Bragg grating refractometer. *Opt. Commun.* **281**(4), 621–625 (2008).
41. Trono, C., Baldini, F., Brenci, M., Chiavaioli, F. & Mugnaini, M. Flow cell for strain- and temperature-compensated refractive index measurements by means of cascaded optical fibre long period and Bragg gratings. *Meas. Sci. Technol.* **22**(7), 075204 (2011).
42. Nakahara, T., Oe, R., Kajisa, T., Taue, S., Minamikawa, T. & Yasui, T. Application of refractive-index-sensing optical frequency comb for biosensing of antigen–antibody reaction," in *Technical Digest of Conference on Lasers and Electro-Optics (CLEO) 2021*, STu2A.2 (2021).
43. Gauglitz, G. Analytical evaluation of sensor measurements. *Anal. Bioanal. Chem.* **410**, 5–13 (2018).
44. Bong, J.-H. *et al.* Pig Sera-derived Anti-SARS-CoV-2 antibodies in surface plasmon resonance biosensors. *Biochip J.* **14**(4), 358–368 (2020).
45. Qiu, G. *et al.* Dual-functional plasmonic photothermal biosensors for highly accurate severe acute respiratory syndrome coronavirus 2 detection. *ACS Nano* **14**(5), 5268–5277 (2020).
46. Moitra, P., Alafeef, M., Dighe, K., Frieman, M. B. & Pan, D. Selective naked-eye detection of SARS-CoV-2 mediated by N gene targeted antisense oligonucleotide capped plasmonic nanoparticles. *ACS Nano* **14**(6), 7617–7627 (2020).
47. Wang, R., Tombelli, S., Minunni, M., Spiriti, M. M. & Mascini, M. Immobilisation of DNA probes for the development of SPR-based sensing. *Biosens. Bioelectron.* **20**(5), 967–974 (2004).
48. Liu, C., Yang, Y. & Wu, Y. Recent advances in exosomal protein detection via liquid biopsy biosensors for cancer screening, diagnosis, and prognosis. *AAPS J.* **20**, 41 (2018).
49. https://web.expasy.org/compute_pi/
50. Di, D., Dileepan, M., Ahmed, S., Liang, Y. & Ly, H. Recombinant SARS-CoV-2 nucleocapsid protein: Expression, purification, and its biochemical characterization and utility in serological assay development to assess immunological responses to SARS-CoV-2 infection. *Pathogens* **10**(8), 1039 (2021).
51. Lu, R.-M. *et al.* Monoclonal antibodies against nucleocapsid protein of SARS-CoV-2 variants for detection of COVID-19. *Int. J. Mol. Sci.* **22**(22), 12412 (2021).
52. Kunishima, M. *et al.* 4-(4, 6-dimethoxy-1, 3, 5-triazin-2-yl)-4-methyl-morpholinium chloride: An efficient condensing agent leading to the formation of amides and esters. *Tetrahedron* **55**(46), 13159–13170 (1999).
53. Kajisa, T. *et al.* Highly sensitive detection of nucleocapsid protein from SARS-CoV-2 using a near-infrared surface plasmon resonance sensing system. *Opt. Continuum* **1**(11), 2336–2346 (2022).

Acknowledgements

The authors acknowledge Prof. Kaoru Minoshima at The University of Electro-Communications, Japan and Dr. Yoshiaki Nakajima of Toho University, Japan for their help in the dual-comb configuration.

Author contributions

T.Y. and T.K. conceived the project. S.M., R.O. T.N., and H.K. developed the dual-comb biosensing system, performed the experiments, and analysed the data. T.K., S.T., Y.T., and S.O. made the MMI fiber biosensor. K.O. and A.S. performed the ELISA experiment. K.Y., T.S., T.M., T.K., S.T., and Tak.Yan. discussed the results and commented on the manuscript. S.M. and T.Y. wrote the manuscript. All authors reviewed the manuscript.

Funding

Japan Society for the Promotion of Science (22H00303); Japan Agency for Medical Research and Development (20he0822006j00); Japan Science and Technology Agency (JPMJMS2025); Cabinet Office, Government of Japan; Tokushima Prefecture.

Competing interests

The authors declare no competing interests.

Additional information

Correspondence and requests for materials should be addressed to T.K. or T.Y.